Chemical Engineering Journal 402 (2020) 126166

Contents lists available at ScienceDirect

Chemical Engineering Journal

journal homepage: www.elsevier.com/locate/cej

Multiscale investigation of adsorption properties of novel 3D printed UTSA-16 structures

Carlos A. Grande[a,*], Richard Blom[a], Vesna Middelkoop[b], Dorota Matras[c], Antonis Vamvakeros[c,d], Simon D.M. Jacques[c], Andrew M. Beale[c,e,f], Marco Di Michiel[d], Kari Anne Andreassen[a], Aud M. Bouzga[a]

[a] SINTEF Industry, Forskningsveien 1, 0373 Oslo, Norway
[b] Vlaamse Instelling voor Technologisch Onderzoek – VITO, Boeretang 200, Mol, Belgium
[c] Finden, Building R71, Harwell Campus, Oxfordshire OX11 0QX, UK
[d] ESRF – The European Synchrotron Radiation Facility, 6 Rue Jules Horowitz, 38000 Grenoble, France
[e] Department of Chemistry, University College London – UCL, London WC1H 0AJ, UK
[f] Research Complex at Harwell, Harwell Science and Innovation Campus, Rutherford Appleton Laboratory, Didcot, Oxon OX11 0FA, UK

HIGHLIGHTS

- 3D printed UTSA-16 monoliths with novel nonaqueous polymer-based formulation.
- XRD-CT operando insight on chemical and structural variation within 3D printed MOF.
- Adsorption of N_2, CH_4, CO_2 and H_2O were measured at three different temperatures.
- Breakthrough curves showing fast diffusion of gases and H_2O easily displacing CO_2.
- Reproducible data near 100% RH: no material degradation or deactivation observed.

GRAPHICAL ABSTRACT

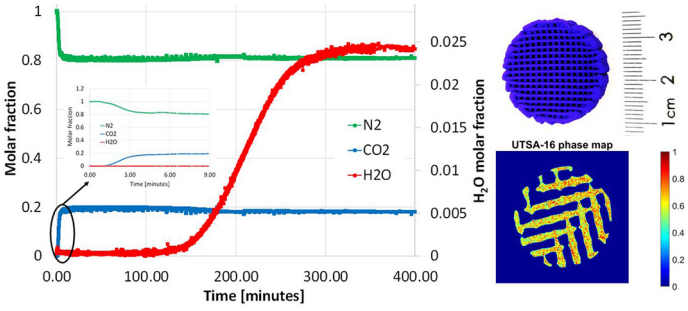

ARTICLE INFO

Keywords:
Carbon dioxide
Water adsorption
Direct write 3D printing
Shaping
In situ operando XRD-CT

ABSTRACT

Structuring MOF materials is a fundamental step towards their commercialization. Herein we report intensive characterization of 3D-printed UTSA-16 monoliths, facilitated by the development of a new non-aqueous ink formulation, employing hydroxypropyl cellulose and boehmite to adjust the rheology of the ink. What makes this formulation and printing process different from the printed adsorbents and catalysts published previously, is that the resulting structures in this work were not sintered. The presence of the binder matrix not only produced the physical properties for printability but also ensured a homogeneous dispersion of UTSA-16 in the structures, as well as gas adsorption characteristics. The monoliths were tested for the adsorption of different gases (N_2, CH_4, CO_2 and H_2O) in order to apply them into separation processes that contribute to defossilizing energy and fuels production. Water is strongly adsorbed in this material (~14 mol/kg at 293 K) and is competing with CO_2 for adsorption sites. Breakthrough curves showed that the retention time of CO_2 decreases significantly when the feed stream is saturated with water. In this study, synchrotron XRD-CT data were collected in situ, in a non-destructive way, and phase distribution maps were reconstructed to, for the first time, gain insight into the spatial and temporal evolution of the UTSA-16 containing phases in the operating 3D printed monolith during the exposure to CO_2.

* Corresponding author.
E-mail address: carlos.grande@sintef.no (C.A. Grande).

https://doi.org/10.1016/j.cej.2020.126166
Received 22 May 2020; Received in revised form 30 June 2020; Accepted 1 July 2020
Available online 08 July 2020

1. Introduction

Metal Organic Frameworks (MOFs) are considered ideal candidate materials for innovative gas separation and adsorption applications involving small gas molecules such as CO_2 and CH_4 [1–5]. Their large internal surface area and the high porosity built up from organic molecules (ligands) and metal nodes or clusters contribute to very large adsorption capacities [6,7].

Adsorption processes are already a mature commercial technology for hydrogen purification and for biogas upgrading. If these technologies are integrated in a system implementing selective CO_2 capture, they can contribute to defossilizing energy and fuel production respectively, mitigating the effect of CO_2 in climate change. An example of successful integration of the existing H_2-PSA has been achieved in Port Arthur refinery. MOF materials applied to these separations can have a significant impact in footprint reduction resulting in improved process economics.

With an increasing number of potential application areas for MOFs, shaping them into particles that can be industrially used is a necessary step for commercialization. Techniques for the production of beads, granules, pellets and monoliths have been reported [8–18]. Another technique that has been gaining momentum in recent years is the production of 3D printed MOF structures [19–26]. It has been previously shown that in several applications of adsorbents and catalysts, structured (geometrically patterned) monoliths have superior performance compared to conventional packed beds, particularly when pressure drop is targeted [27–29].

Metal-organic framework UTSA-16, $K(H_2O)_2Co_3(cit)(Hcit)$ (Hcit = citric acid), has been shown to possess one of the highest loadings of CO_2 per volume of adsorbent [30–32]. There are two main reasons for this:

- The favourable interactions between CO_2 and disordered water sites occupying large pores in the material (each K + ion coordinates two structural water molecule sites at ambient pressure) [31,33,34].
- The density of UTSA-16 crystals is 1.659 g/cm^3 and the particle density is close to zeolites, which means that the weight of UTSA-16 packed in a fixed column volume is higher than other MOFs [11].

To produce shaped structures of UTSA-16 it is essential to ensure that the printing suspensions contain at least 50% of alcohol (ethanol, propanol, etc) in all steps of the production [11]. The difficulty in the shaping is that such alcohols have a very different evaporation rate than water. Most recently, stable performance and relatively good adsorption kinetics of 3D-printed UTSA-16 monoliths with 85 wt% MOF content was reported [26]; a CO_2 adsorption capacity of 1.31 mmol/g was obtained, which is equivalent to 87% of the powder capacity under the same conditions (5000 ppm of CO_2 at 25 °C).

In the current work, UTSA-16 monoliths produced by 3D printing were fully investigated for their use within adsorption processes. The material was characterized by X-Ray diffraction, thermo-gravimetric analysis and scanning electron microscopy. More insight into the crystal structure and spatial and temporal distribution across the adsorbing 3D printed UTSA-16 monolith was gained by performing in situ high-energy X-ray Diffraction Computed Tomography (XRD-CT) studies. The present study is the first of its kind to explore adsorption in an operating 3D printed MOF monolith combining the use of in situ/*operando* XRD-CT under a CO_2 flow. In a previous synchrotron *operando* study by the authors, XRD-CT was employed to provide information on the spatial distribution of the active phase in a working 3D printed catalyst monolith for CO_2 methanation [35]. The 5D XRD-CT imaging technique, combined with new fast tools for simultaneous data collection and analysis allow for the chemistry inside working reactors to be imaged, assessing the fidelity of (3D printed) material design and determine the chemical and physical form of active components [36]. In terms of applications prospects, we measured the adsorption equilibrium of CO_2, CH_4, N_2 and H_2O at three different temperatures (293, 313 and 343 K). We also measured breakthrough curves of CO_2-N_2 and CO_2-N_2-H_2O mixtures.

2. Experimental

UTSA-16 was synthesized following a previously reported recipe [30,31]. The hydrothermal ynthesis was done using the following compounds: $Co(OAc)_2$, $4H_2O$,$C_6H_8O_7$, H_2O, KOH, H_2O and C_2H_5OH, which were put in a Teflon-lined 5L Parr autoclave reactor in a molar ratio of 1:1:3:139:43. The reactor was heated to 393 K and kept at that temperature for 2 days before letting it cool down to ambient temperature. Over 100 g of UTSA-16 powder was produced in each batch using these molar ratios.

The formulation of the ink in this work was based on non-aqueous solvent to avoid possible interaction of water molecules with the UTSA-16's citrate ligands for prolonged periods of time. The preparation of the printing ink of the UTSA-16 polymer composites was carried out using the tuneable rheology of an adequate selection of precursors: 45 wt% of a 6% hydroxypropyl cellulose (HPC) solution with isopropyl alcohol (IPA) and 18 wt% nanosized Boehmite AlO(OH) based dispersant.

The printing formulation has been developed by taking into account the effect of blending parameters (such as the stepwise addition of solid precursors, rotational speed in a planetary mixer and constant ambient temperature) to ensure sufficient dispersion of the active UTSA-16 material throughout the polymer micro-lattices.

The direct-write 3D printing of the multi-material ink (consisting of active UTSA-16, with HPC/IPA solution and AlO(OH) as binders) involved its micro extrusion and fibre deposition through a nozzle by print head movement in *xyz*. The UTSA-16 containing ink was printed into 3D periodic ('log pile') cylindrical structures with a diameter of 28 mm using a high-end nScrypt 3D-450HP printer (see Fig. 1). The printed cylinders were subsequently slowly dried in a controlled

Fig. 1. 3D printed UTSA-16 monoliths: (a) consistent periodic structures produced by tuning the formulation and nScrypt 3D printing parameters and (b) image of an as-fabricated cylinder with a diameter of ca. 2.5 cm after drying.

humidity environment and at ambient temperature. The final monoliths all have the same final composition (Table S1 in ESI summarises the dry solids content of the monoliths). The current adsorbent monolith preparation method differs from the ones that were previously described [37,38] in that the UTSA-16-loaded polymer matrix was not removed – no thermal treatment was applied allowing the entire composite cylinder to densify into a solid bulk to achieve the final shape.

The thermal stability of the UTSA-16 monoliths was analysed by using a TG-DSC-MS instrument (Netzsch STA 449 F1 instrument equipped with a QMS 403C MS analyser). Experiments were carried out using approximately 30 mg pieces of the monolith, 2 K/min heating rate and a nitrogen flow of 50 ml/min. The samples were heated to 1073 K. Mass changes (TG), heat transfer within the sample (DSC) as well as analyses of the kind of volatile components leaving the sample during the process (by mass spectrometry - MS) were recorded.

Subsequently, XRD-CT measurements were performed on a 3D printed UTSA-16 monolith after exposure to pure CO_2 at a flow rate of 100 ml/min. The XRD-CT measurements were carried out at the ID15A beamline at ESRF using a monochromatic beam with an energy of 90 keV focused to a spot size of 40 μm × 20 μm (Horizontal × Vertical). XRD-CT scans were collected using a zigzag approach over a total angular range of 180° in steps of 0.721° (i.e. 250 angular steps) combined with translational steps of 40 μm (with a total number of 320 steps across 12.8 mm) using a Pilatus3 X CdTe 2 M detector. Each complete XRD-CT scan comprised 80,000 diffraction patterns. The total acquisition time per point was 20 msec and each XRD-CT scan lasted for a total of ca. 20 min. The detector calibration was performed using a CeO_2 NIST standard. Every 2D diffraction image was converted to a 1D powder diffraction pattern after applying a 10% trimmed mean filter to remove outliers using the nDTomo and pyFAI software packages [39–42]. The data integration was performed with a fast GPU processor. The final XRD-CT images (i.e. reconstructed data volume) were obtained using the filtered back projection algorithm; see the resulting tomographic reconstructions in Figure X corresponding to peak intensity, position and FWHM constructed after peak fitting for the first three diffraction reflections (1 0 1), (1 1 2) and (2 0 0). To obtain a clearer view of the changes in the three peak parameters the ratio of these maps was calculated, and histograms plotted for each individual peak.

Conventional lab X-ray diffraction (XRD) measurements were performed using a Philips/Panalytical X'Pert Pro diffractometer set up in Bragg-Brentano geometry with Cu Kα source with $\lambda = 1.5418$ Å at 40 kV and 40 mA at room temperature. Powder X-Ray diffraction patterns from $2\Theta = 5$ to 50 of the MOF adsorbent were measured using a PANalytical EMPYREAN diffractometer equipped with a Cu-source and Pixel 3D detector.

To determine microstructure and composition, Scanning Electron Microscopy (SEM) and Energy Dispersive X-ray (EDX) spectroscopy images were obtained using a FEI Nova NanoSEM 450 field emission gun (FEG), operated at an accelerating voltage of 25 keV, and fitted with a Bruker QUANTAX 200 EDX system and XFlash 5030 SDD detector.

Adsorption isotherms of pure gases were measured in a Belsorp Max manometric unit. Nitrogen isotherms at 77 K were used for the estimation of the BET surface area. Isotherms for CO_2, CH_4 and N_2 were measured at 293, 313 and 343 K up to 101 kPa. For water, measurements were carried out until its saturation partial pressure or to a maximum of 4 kPa. The adsorbent was degassed overnight at 393 K under vacuum before the measurements. Adsorption equilibrium data was fitted with the Virial isotherm. A theoretical description of the isotherm and parameters used for the fitting are given in the Supplementary information.

Breakthrough curves of the binary (CO_2-N_2) and ternary (H_2O-CO_2 and N_2) mixtures were measured in a standard unit for measuring dynamic experiments. A more detailed description is given in the Supplementary Information. For that purpose, two 3D-printed structures (each with 19 mm diameter and 9 mm length and weight of 3.7103 g) were introduced into a one-inch stainless steel tube. Prior to the experiments, the material was degassed at 393 K under a constant flow of helium that was also passed through the adsorbent before starting the breakthrough curves. The experiments were made with a total flowrate of 100 ml/min composed by 20% CO_2 and 80% N_2. For the experiment with water, a saturator was used, and the flowrate and gas composition was maintained (same molar fraction in dry basis). The real molar fractions are affected by the 2.2% of water introduced in the experiments.

3. Results and discussions

3.1. Adsorbent characterization

What makes this formulation and printing process different from those published previously is that the resulting structures in this work were not sintered, and the sacrificial material was not removed. Typically, 'green' printed structures are subjected to debinding and sintering processes to completely combust the organic binders and free up sorption sites, ensuring the process results in the least possible effect on the final structure integrity. The current work avoided any additional processing steps preserving the inter-particle cohesion and mechanical robustness while keeping a reduction in the surface area to a minimum. While retaining the functionality, the present binder matrix

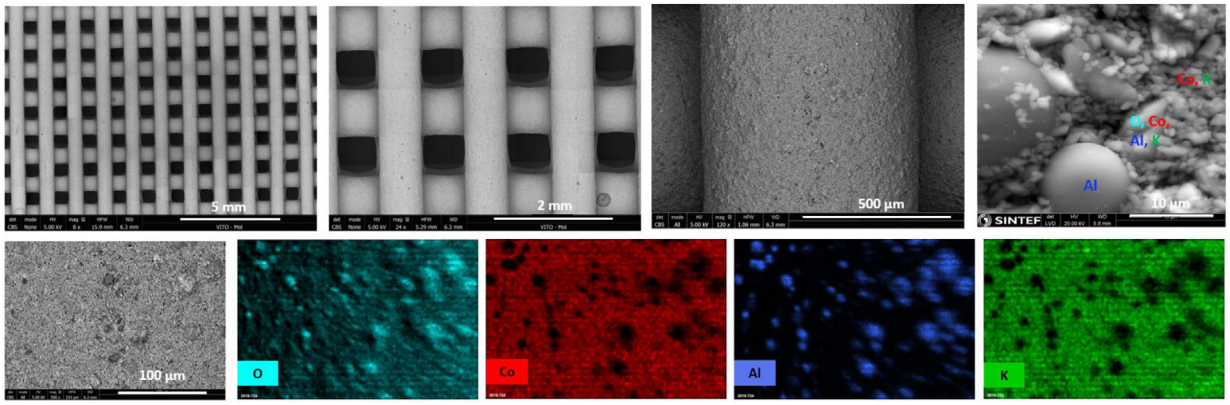

Fig. 2. SEM images of macro and microstructure (top, bottom left) and corresponding EDX compositional images/elemental maps (bottom) of 3D printed monoliths composed of well-dispersed UTSA-16, $K(H_2O)_2Co_3$(cit)(Hcit) and Boehmite (AlO(OH)) dispersant in non-aqueous binder; scale bars indicate 5 mm, 2 mm, 500 μm, 10 μm and 100 μm respectively from left to right; top right spot analysis and the bottom row elemental mapping show the UTSA-16 species and dispersant particles in the surrounding binder matrix at higher magnification.

not only facilitated physical properties for printability but also enabled gas diffusion and adsorption characteristics.

3D printed monoliths maintained a porous structure after solidification and a considerably higher BET surface area of 540 m^2/g. Table S2 in ESI provides a summary of the Nitrogen adsorption measurements at 77 K and obtained pore size profiles. The measured isotherm for a 3D printed monolith sample can be found in Fig. S1. The nitrogen adsorption measurements on the 3D printed monoliths produced Type II-isotherm curves during the initial stage, which was subsequently, however, similar to the Type IV isotherm containing a hysteresis loop of Type H4 [43]. The hysteresis loop relates to a marked increase in N_2 adsorption over a relative pressure range of 0.4–0.8. While Type II is the most common isotherm for nonporous and macroporous adsorbents, Type IV is indicative of the presence of mesoporous structures that greatly vary in shape and are associated with subtle changes in adsorption and desorption behaviour. In addition, the H4 hysteresis corresponds to capillary condensation in the mesopores that are slit-shaped and, in terms of size, closer to the micropore region.

SEM images in Fig. 2 show the macro- and micro-structure of 3D printed UTSA-16 containing monoliths prior to the adsorption measurements. HPC polymer binder and Boehmite-based additives were employed as support materials in order to tailor the plasticity and mechanical properties of the resulting 3D printed composite monoliths as well as their physico-chemical functionality (diffusion pathways and surface properties). Elemental EDX point analysis and EDX maps reveal UTSA-16 constituents (Co and K species) uniformly dispersed within the binder matrix and discrete regions of Boehmite (AlO(OH) features and particles of up to 20 μm in size) across the 3D printed fibres. For elemental composition analysis, see the individual EDX spectra from across the representative regions of the 3D printed fibre in Fig. S2 in ESI.

Figs. S3 and S4 in ESI present ex-situ lab XRD data on the original UTSA-16 powder as well as 3D printed UTSA-16 monoliths before and after CO_2 adsorption. The unit cell parameters correspond to those obtained in the literature (13.0691(4) Å b 13.0691(4) Å c 30.1570(10) Å) [34]. The changes of the a, b and c parameters in the orthorhombic phase before and after CO_2 adsorption are shown in Table S3 (ESI).

The in situ XRD-CT measurements confirmed the crystal structure and unit cell parameters' changes in the bulk material upon adsorption, measured by the lab XRD instrument (See Figs. S5 and S6 in ESI for further details). This was followed by a detailed comparison of the spatial distribution of peak intensities, peak position and FWHM, measured across a horizontal cross section in the 3D printed UTSA-16 monolith using high energy X-ray diffraction at the ID15A beamline. On introducing 100 ml/min CO_2 into the tubular reactor, structural changes were observed for all three main reflections (101, 112 and 200). The combined data on the phase distribution maps were constructed to provide more detailed information on physical or chemical spatial variations. The distribution maps in Fig. 3 feature some spatial (local) variations in concentrations of all three phases and changes in peak intensity, peak position and FWHM. All the three sets of in situ XRD-CT data suggested that the overall behaviour is consistent across all three reflections revealing that the 3D printed UTSA-16 adsorbent evolved under CO_2 conditions. There is an apparent increase in peak intensity and peak positions. The shifts in 2θ peak point to changes in lattice parameters following adsorption, availability of adsorption sites and the possible presence of intercalated H_2O molecules. The trend in these changes are evidenced by the ratios of intensities of the parameters before and after the exposure to CO_2 for the three main reflections (see relative changes in histograms in Fig. S6).

3.2. Thermal stability of UTSA-16 monolith

The TG-DSC-MS traces during heating at a heating rate of 2 °C/min to 800 °C is shown in Fig. 4. Below 100 °C, adsorbed water is released, shown by an endothermic DSC signal and an increase in the MS water signal. At around 100 °C, the TG trace reaches a flat plateau indicating that most water has been desorbed before the mass trace starts falling between 150 and 200 °C. This first reduction in mass is caused by a part of the samples being combusted by the traces of molecular oxygen within the instrument: a small exothermal peak in the DSC curve is accompanied by a sharp reduction in the O_2 level and an increase in the CO_2 level. At around 330 °C there is a sharp endothermic peak caused by the total decomposition of the material. This peak is accompanied by sharp releases of CO_2, H_2O and also small amounts of O_2. After the decomposition, the mass trace levels off, flattening out at 53.1% of the initial mass. Assuming that UTSA-16 decomposes to the metal oxides (CoO and K_2O), the amount of Al-oxide dispersant can be estimated at around 18 wt%.

3.3. Adsorption equilibrium

The adsorption equilibrium of N_2, CH_4, CO_2 and H_2O measured at

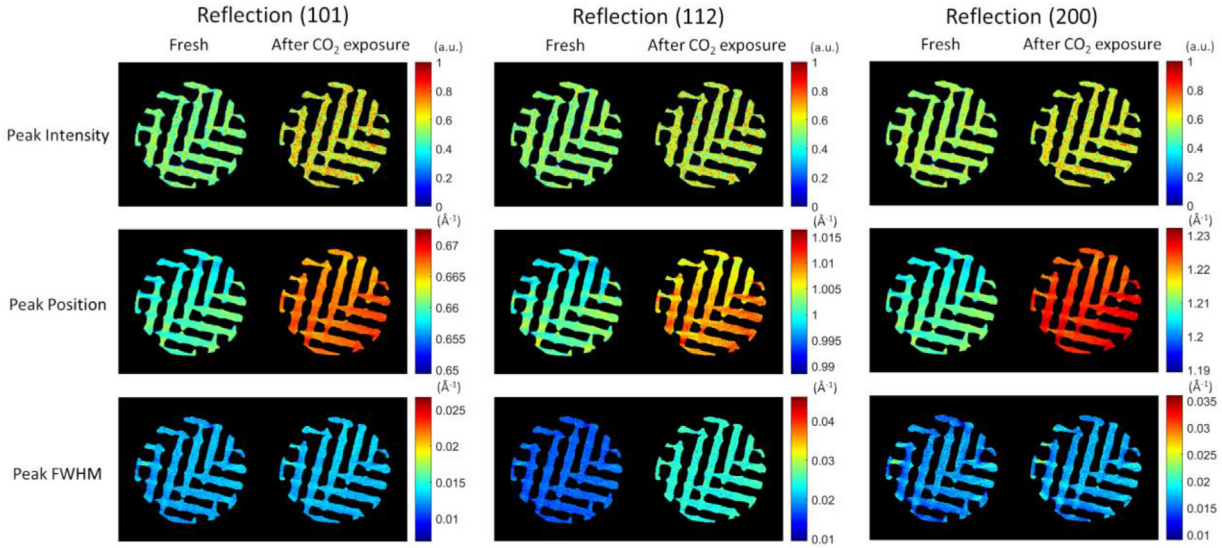

Fig. 3. Structural evolution and active sites distribution across the polymer matrix of 3D printed monolith with peak intensity, peak position and FWHM spatial distribution across a representative cross section for three main *UTSA-16* reflections (200, 101, 112) before and after CO_2 adsorption has taken place.

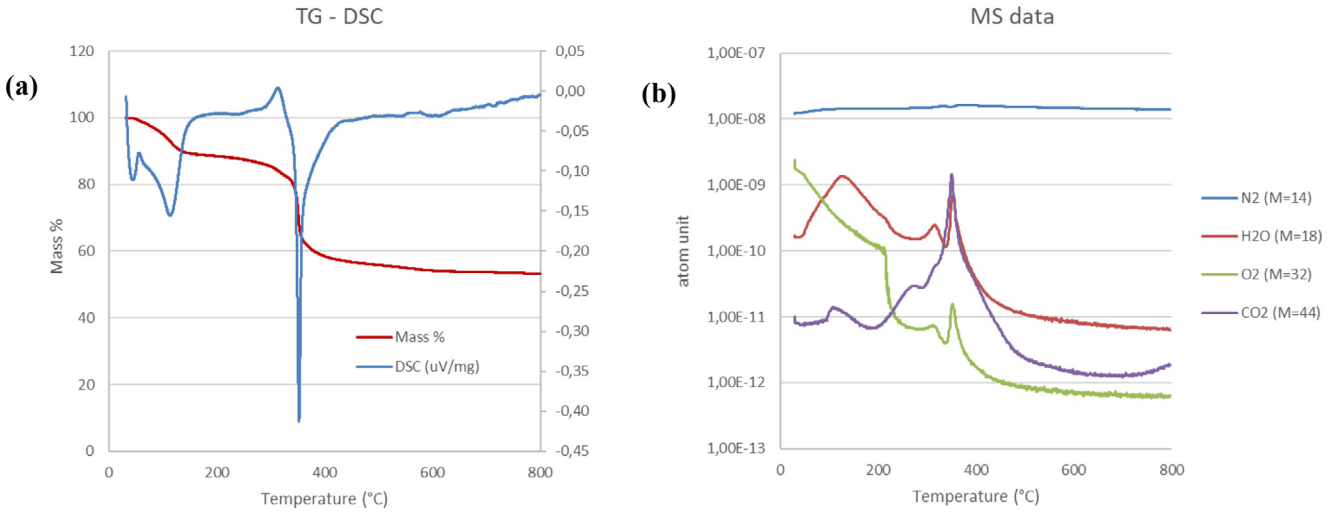

Fig. 4. TG + DSC data (a) and MS traces (b) from thermal decomposition experiments of UTSA-16 3D printed monoliths under nitrogen atmosphere.

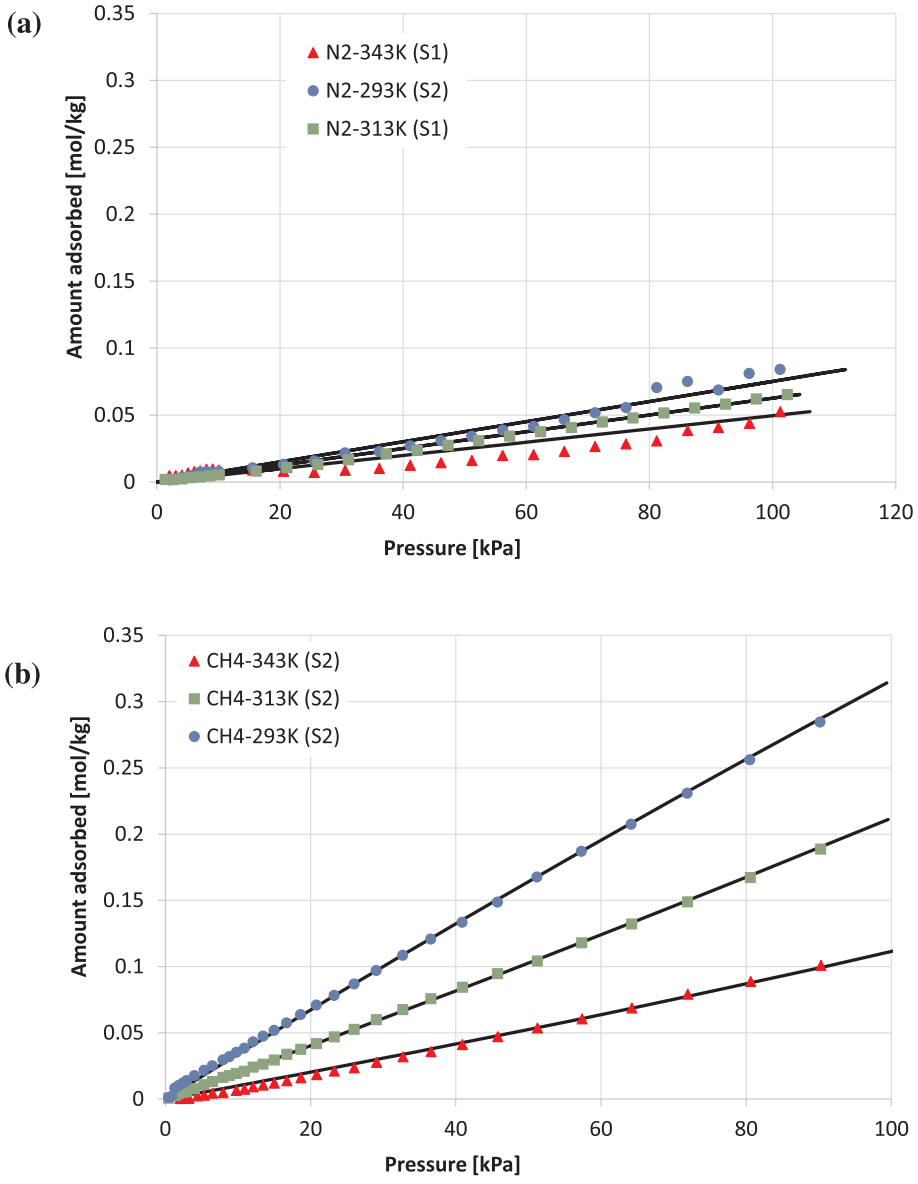

Fig. 5. Adsorption equilibrium isotherms of N_2 (a) and CH_4 (b) on 3D-printed UTSA-16 monolith at 293, 313 and 343 K. Solid lines are the fitting of the Virial model.

293, 313 and 343 K is shown in Figs. 5 and 6. Measurements were carried out on two samples (denoted as S1 and S2) coming from different monoliths produced with the same batch. The results indicate that the difference of amount adsorbed of carbon dioxide in the two samples is small and less pronounced in the Henry zone of the isotherms. The amount of nitrogen adsorbed is very small and is linear within the whole region. Methane is adsorbed stronger than nitrogen and the isotherms are only slightly non-linear at pressures closer to atmospheric. Carbon dioxide is more selectively adsorbed reaching a loading of 2.5 mol/kg at 298 K and atmospheric pressure. Water is the most strongly adsorbed gas reaching a capacity of 14 mol/kg at 293 K at almost 100% relative humidity (corresponding to 2.1 kPa). Moreover, the water isotherms are not Type I according to IUPAC classification. Since they present multiple inflection points in different locations depending on the temperature used for the measurements, it is necessary to use many parameters to describe them. The solid lines in the figures are the fitting of the Virial model. It can be seen that the level of complexity of the model depends on the shape of the isotherms; there are such a high number of parameters in the description of the water isotherms, that it is probably not correct to extrapolate the data.

The capacity of CO_2 and water is around 60% compared to the reported data on the UTSA-16 powder [32]. Reduction of capacity and surface area was also reported after shaping [44,45]. Comparing UTSA-16 with other commercial materials, the CO_2 capacity is intermediate, ranging between that of zeolite 13X and activated carbon [46–48]. The main advantage of UTSA-16 is that the isotherms of CO_2 are not as steep as those of zeolite 13X which can result in less power consumption for regeneration.

3.4. Breakthrough curves

To show how the samples will perform with real mixtures, we have measured binary and ternary breakthrough curves. In Fig. 7, the results of a CO_2-N_2 breakthrough curve is displayed. It is seen that the sample

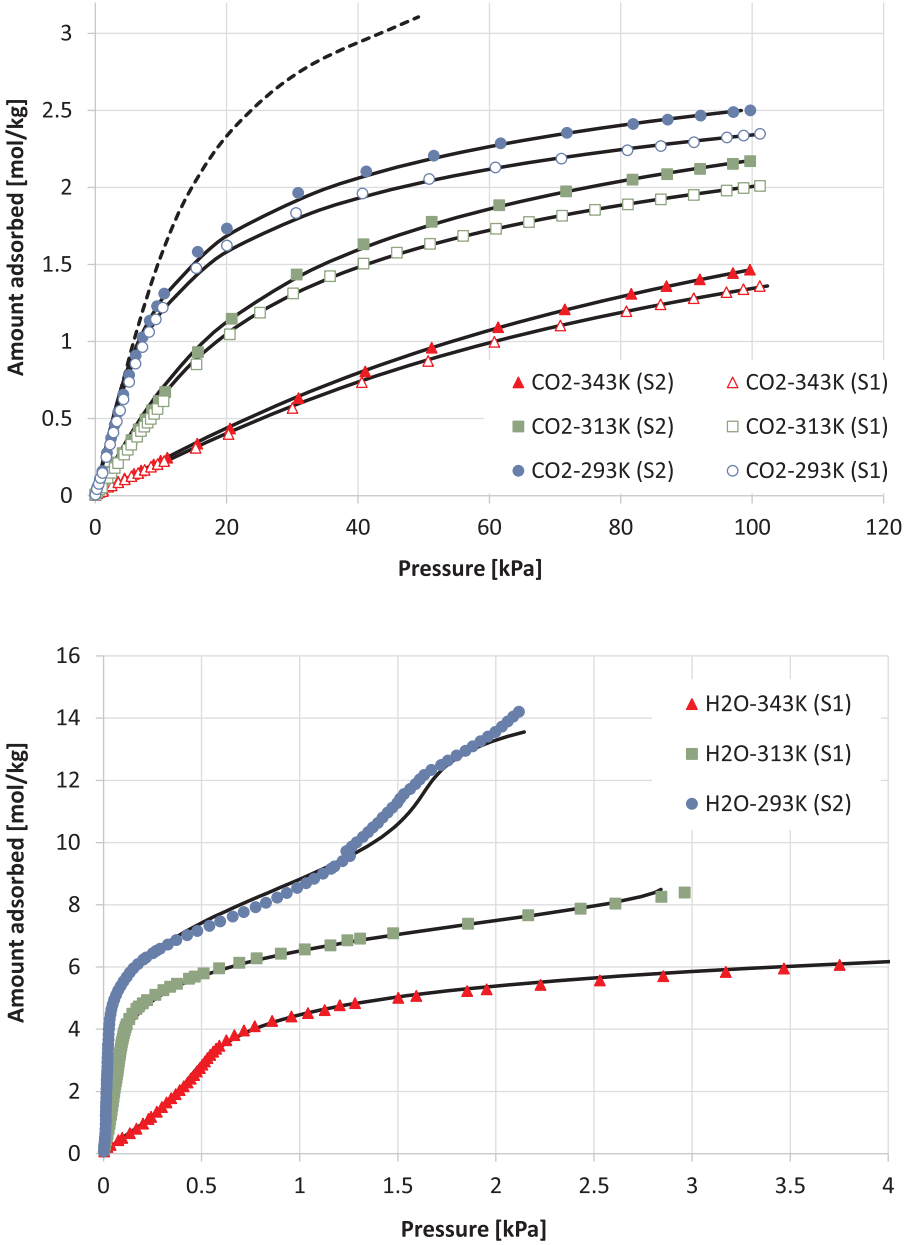

Fig. 6. Adsorption equilibrium isotherms of CO_2 (a) and H_2O (b) on 3D-printed UTSA-16 monolith at 293, 313 and 343 K. Solid lines are the fitting of the Virial model.

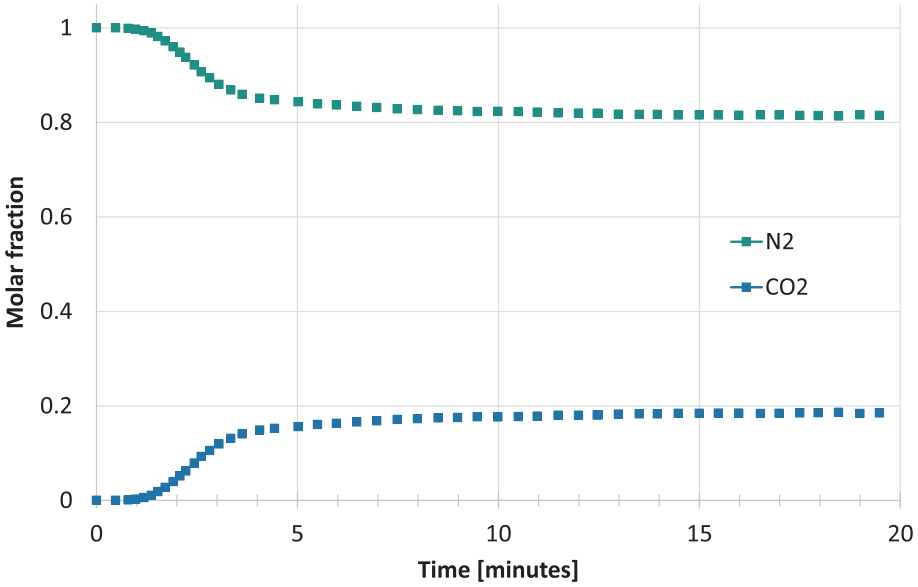

Fig. 7. Binary breakthrough curve with 20% of CO_2 and 80% N_2 at 343 K.

is able to selectively retain CO_2 over nitrogen. The shape of the curve indicates a rather steep breakthrough of CO_2 which shows that dispersion and diffusional effects are not large. Moreover, there is a longer tail in the curve that is frequently caused by thermal effects; the adsorption of CO_2 is exothermic which results in a net increase of the temperature of the adsorbent reducing its CO_2 capacity. While the adsorbent is saturated at the local (slightly higher) temperature, the gas starts to cool down increasing its capacity and adsorbing more CO_2 until the equilibration at the right temperature is achieved. The shape of the breakthrough does not show any kind of anomalous shape due to the defects in the 3D printing of the material.

The results of the ternary breakthrough water of H_2O-CO_2-N_2 are presented in Fig. 8. When water is present in the feed stream, the breakthrough time of CO_2 is comparable to the one in the dry experiments once that the water concentration front moves much slower than the CO_2 front. However, the CO_2 plateau moves back to the feed concentration once that water gets adsorbed indicating that CO_2 is displaced by water. The experiments were performed twice and no difference in the results were observed. It has been hypothesised by Masala et al [31], that CO_2 adsorption can be attributed to K^+ species, forming $K^+(CO_2)$ and $K^+(CO_2)_2$ adducts – rather than that being a water-directed interaction. There were initial concerns that working with the feed stream containing close to 100% relative humidity could cause the structure of the material to be damaged, but according to the measurements, the experiments were reproducible, and no material degradation or deactivation was observed.

4. Conclusions

We report the development of a new non-aqueous cellulose-based ink formulation, and successful 3D-printing of UTSA-16 composite monoliths. The rheology of the ink used for printing was adjusted by adding an appropriate quantity of hydroxypropyl cellulose and boehmite. The monoliths contained 18% of boehmite. The surface area of the 3D-printed sample is ~540 m^2/g indicating a reduction of 30% when compared to the powder used. Gas diffusion pathways through

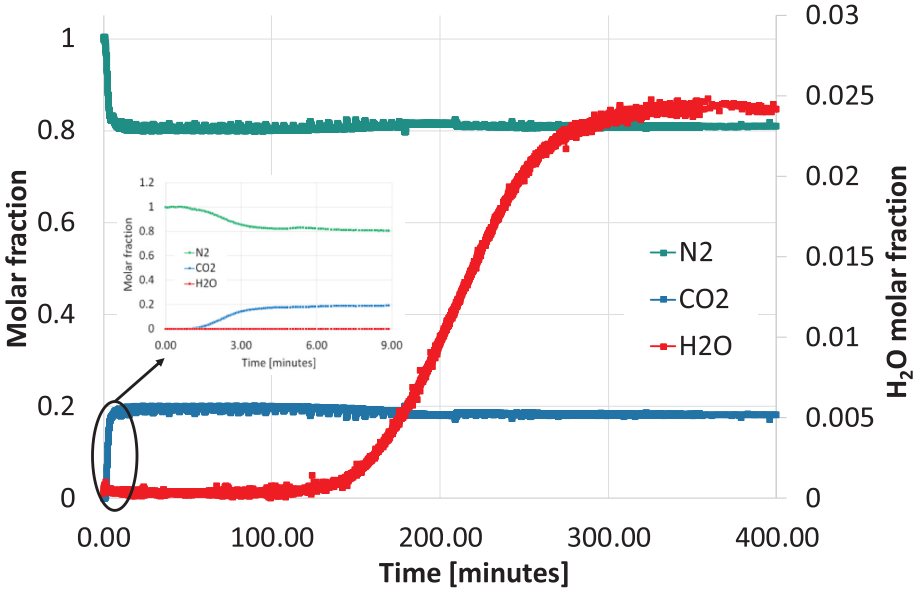

Fig. 8. Ternary breakthrough curve with 2.2% H_2O, 19.6% of CO_2 and 78.2% N_2 at 343 K.

the microstructure of the monoliths were not limited by the presence of the polymer matrix. Adsorption of N_2, CH_4, CO_2 and H_2O were measured at three different temperatures up to atmospheric pressure (or 4 kPa for water). The isotherms of nitrogen are linear in the 0–100 kPa region, while methane is slightly nonlinear, with a small amount adsorbed (0.3 mol/kg at 293 K and 100 kPa). Carbon dioxide loading is 2.5 mol/kg at 100 kPa and 293 K and 1 mol/kg at 10 kPa indicating that the isotherm is not very steep. This is crucial for reducing the power consumption of regeneration in adsorption processes. The amount of water at 293 K at saturation pressure is 14 mol/kg and the isotherms of water are not Type I IUPAC classification. The breakthrough curves showed that the diffusion of gases is fast and water can easily displace carbon dioxide. This confirms that water competes with CO_2 for adsorption sites. The 3D-printed monolith was used for several breakthrough measurements with water and there was no degradation or reduction of capacity observed during the experimental campaign.

In situ synchrotron XRD-CT was employed to gain complementary information pertinent to the spatial and temporal evolution of the UTSA-16 phases in the 3D printed monolith during adsorption under a flow of CO_2 at ambient pressure. The XRD-CT data were analysed and plotted to reconstruct phase distribution maps of each parameter (diffracted intensity of selected peak area, peak position, and peak width) across a representative slice in the 3D printed monolith. A complete understanding of the structure response and distribution of the active phases under operating conditions is crucial to providing scope for the further optimisation of adsorbent design, properties and performance.

Declaration of Competing Interest

The authors declare that they have no known competing financial interests or personal relationships that could have appeared to influence the work reported in this paper.

Acknowledgments

The authors acknowledge the support of the Research Council of Norway through the CLIMIT program by the SINTERCAP project (233818). In addition, this publication has been produced with support from the BIGCCS Centre, performed under the Norwegian research program Centres for Environment-friendly Energy Research (FME). Furthermore, the authors acknowledge the following partners for their contributions: ConocoPhillips, Gassco, Shell, Statoil, TOTAL, GDF SUEZ and the Research Council of Norway (193816/S60).

The authors would like to thank the ESRF for the beamtime (proposal CH5329), and the staff of beamline ID15A for their assistance with the acquisition of the XRD-CT data presented in this paper. The authors also gratefully acknowledge VITO research staff who assisted with this study: Jo Verwimp (3D printing), Myrjam Mertens (lab XRD) and Raymond Kemps (SEM/EDX).

Appendix A. Supplementary data

Supplementary data to this article can be found online at https://doi.org/10.1016/j.cej.2020.126166.

References

[1] O.M. Yaghi, M. O'Keeffe, N.W. Ockwig, H.K. Chae, M. Eddaoudi, J. Kim, Reticular synthesis and the designof new materials, Nature 423 (2003) 705–714, https://doi.org/10.1038/nature01650.

[2] O.M. Yaghi, H. Li, C. Davis, D. Richardson, T.L. Groy, Synthetic strategies, structure patterns, and emerging properties in the chemistry of modular porous solids, Acc. Chem. Res. 31 (1998) 474–484, https://doi.org/10.1021/ar970151f.

[3] P. Nugent, Y. Belmabkhout, S.D. Burd, A.J. Cairns, R. Luebke, K. Forrest, T. Pham, S. Ma, L. Wojtas, M. Eddaoudi, M.J. Zaworotko, Porous materials with optimal adsorption thermodynamics and kinetics for CO2 separation, Nature 495 (2013) 80–84, https://doi.org/10.1038/nature11893.

[4] P. Horcajada, C. Serre, M. Vallet-Regí, M. Sebban, F. Taulelle, G. Ferey, Metal–organic frameworks as efficient materials for drug delivery, Angew. Chem. Int. Ed. 45 (2006) 5974–5978, https://doi.org/10.1002/anie.200601878.

[5] S. Horike S. Shimonura S. Kitagawa Soft porous crystals Nat. Chem. 1 (2009) 695–704, 2009. 10.1038/nchem.444.

[6] C.A. Trickett, A. Helal, B.A. Al-Maythalony, Z.H. Yamani, K.E. Cordova, O.M. Yaghi, The chemistry of metal–organic frameworks for CO2 capture, regeneration and conversion, Nat. Rev. Mater. 2 (2017) (2017) 17045, https://doi.org/10.1038/natrevmats.2017.45.

[7] E.J. Carrington, C.A. McAnally, A.J. Fletcher, S.P. Thompson, M. Warren, L. Brammer, Solvent-switchable continuous-breathing behaviour in a diamondoid metal–organic framework and its influence on CO2 versus CH4 selectivity, Nat. Chem. 2 (2017) 882–889, https://doi.org/10.1038/nchem.2747.

[8] M. Gaab, C. Eichholz, M. Kostur, U. Müller, S. Maurer. Metal-organic framework extrudates with high packing density and tunable pore volume. US Patent 9,370,771, 21 Jun 2016.

[9] D.W. Lee, T. Didriksen, U. Olsbye, R. Blom, C.A. Grande, Shaping of metal-organic framework UiO-66 using alginates: effect of operation variables, Sep. Purif. Technol. 235 (2020) 116182, , https://doi.org/10.1016/j.seppur.2019.116182.

[10] P. Kusgens, A. Zgaverdea, H. Fritz, S. Siegle, S. Kaskel, Metal-organic frameworks in monolithic structures, J. Am. Chem. Soc. 93 (2010) 2476–2479, https://doi.org/10.1111/j.1551-2916.2010.03824.x.

[11] C.A. Grande, V. Águeda, A. Spjelkavik, R. Blom, An efficient recipe for formulation of metal-organic frameworks, Chem. Eng. Sci. 124 (2015) 154–158, https://doi.org/10.1016/j.ces.2014.06.048.

[12] A. Spjelkavik, Aarti, S. Divekar, T. Didriksen, R. Blom. Forming MOFs into spheres by use of molecular gastronomy methods. Chem. Eur. J. 20 (2014) 8973-8978. https://doi.org/10.1002/chem.201402464.

[13] W.H. Hong, S.P. Perera, A.D. Burrows, Manufacturing metal-organic framework monoliths and their applications in CO2 adsorption, Microp. Mesop. Mater. 214 (2015) 149–155, https://doi.org/10.1016/j.micromeso.2015.05.014.

[14] G.W. Peterson, J.B. DeCoste, T. Grant Glover, Y. Huang, H. Jasuja, K.S. Walton, Effect of pelletization pressure on the physical and chemical properties of the metal-organic frameworks Cu3(BTC)2 and UiO-66, Microp. Mesop. Mater. 179 (2013) 48–53, https://doi.org/10.1016/j.micromeso.2013.02.025.

[15] A.H. Valekar, K.-H. Cho, U.-H. Lee, J.S. Lee, J.W. Yoon, Y.K. Hwang, S.G. Lee, S. Cho, J.-S. Chang, Shaping of porous metal-organic framework granules using porous p-alumina as binder, RSC Adv. 7 (2017) 55767, https://doi.org/10.1039/C7RA11764G.

[16] S. Cavenati, C.A. Grande, A.E. Rodrigues, C. Kiener, U. Müller, Metal organic framework adsorbent for biogas upgrading, Ind. Eng. Chem. Res. 47 (2008) 6333–6335, https://doi.org/10.1021/ie8005269.

[17] D. Crawford, J. Casaban, R. Haydon, N. Giri, T. McNally, S.L. James, Synthesis by extrusion: continuous, large-scale preparation of MOFs using little or no solvent, Chem. Sci. 6 (2015) 1645–1649, https://doi.org/10.1039/C4SC03217A.

[18] J. Ren, N.M. Musyoka, H.W. Langmi, A. Swartbooi, B.C. North, M. Mathe, A more efficient way to shape metal-organic framework (MOF) powder materials for hydrogen storage applications, Int. J. Hydrogen Energy 2015 (2015) 4617–4622, https://doi.org/10.1016/j.ijhydene.2015.02.011.

[19] J. Dhainaut, M. Bonneau, R. Ueoka, K. Kanamori, S. Furukawa, "Formulation of metal–organic framework inks for the 3D printing of robust microporous solids toward high-pressure gas storage and separation, ACS Appl. Mater. Interf. 12 (2020) 10983–10992, https://doi.org/10.1021/acsami.9b22257.

[20] G.J.H. Lim, Y. Wu, B.B. Shah, J. Koh, C.K. Liu, D. Zhao, A.C. Cheetham, J. Wang, J. Ding, "3D-Printing of pure metal–organic framework monoliths, ACS Mater. Lett. 1 (2019) 147–153, https://doi.org/10.1021/acsmaterialslett.9b00069.

[21] S. Hock, M. Rose, 3D-structured monoliths of nanoporous polymers by additive manufacturing, Chem. Ing. Tech. 92 (2020) 1–8, https://doi.org/10.1002/cite.201900149.

[22] M. Bible, M. Sefa, J.A. Fedchak, J. Scherschligt, B. Natarajan, Z. Ahmed, M.R. Hartings, 3D-printed acrylonitrile butadiene styrene-metal organic framework composite materials and their gas storage properties. 3D Print, Add. Manuf. 5 (2018) 63–72, https://doi.org/10.1089/3dp.2017.0067.

[23] S. Sultan, H.N. Abdelhamid, X. Zou, A.P. Mathew, CelloMOF: nanocellulose enabled 3D printing of metal-organic frameworks, Adv. Funct. Mater. 29 (2019) 1805372, https://doi.org/10.1002/adfm.201805372.

[24] S. Couck, J. Lefevere, S. Mullens, L. Protasova, V. Meynem, G. Desmet, G.V. Baron, J.F.M. Denayer, "CO2, CH4 and N2 separation with a 3DFD-printed ZSM-5 monolith, Chem. Eng. J. 308 (2017) 719–726, https://doi.org/10.1016/j.cej.2016.09.046.

[25] F. Rezaei, S. Lawson, H. Hosseini, H. Thakkar, A. Hajari, S. Monjezi, A.A. Rownaghi, "MOF-74 and UTSA-16 film growth on monolithic structures and their CO2 adsorption performance, Chem. Eng. J. 313 (2017) 1346–1353, https://doi.org/10.1016/j.cej.2016.11.058.

[26] H. Thakkar, S. Eastman, Q. Al-Naddaf, A.A. Rownaghi, F. Rezaei, "3D-printed metal-organic framework monoliths for gas adsorption processes, ACS Appl. Mater. Interfaces 41 (2017) 35908–35916, https://doi.org/10.1021/acsami.7b11626.

[27] Shane Lawson, Qasim Al-Naddaf, Anirduh Krishnamurthy, Marc St. Amour, Connor Griffin, Ali A. Rownaghi, James C. Knox, Fateme Rezaei, UTSA-16 growth within 3D-printed Co-kaolin monoliths with high selectivity for CO 2/CH 4, CO 2/N 2, and CO 2/H 2 separation, ACS Appl. Mater. Interfaces 10 (22) (2018) 19076–19086, https://doi.org/10.1021/acsami.8b05192.

[28] N.F. Bastos-Rebelo, K.A. Andreassen, L.I. Suarez Ríos, J.C. Piquero Camblor, H.-J. Zander, C.A. Grande, Pressure drop and heat transfer properties of cubic isoreticular foams, Chem. Eng. Proc. Process Intensif. 127 (2018) 36–42, https://doi.org/10.1016/j.cep.2018.03.008.

[29] S. Lawson, B. Adebayo, C. Robinson, Q. Al-Naddaf, A.A. Rownaghi, F. Rezaei, The

effects of cell density and intrinsic porosity on structural properties and adsorption kinetics in 3D-printed zeolite monoliths, Chem. Eng. Sci. 218 (2020) 115564, , https://doi.org/10.1016/j.ces.2020.115564.
[30] S. Xiang, X. Wu, J. Zhang, R. Fu, S. Hu, X. Zhang, A 3D canted antiferromagnetic porous metal−organic framework with anatase topology through assembly of an analogue of polyoxometalate, J. Am. Chem. Soc. 127 (2005) 16352–16353, https://doi.org/10.1021/ja0546065.
[31] A. Masala, J.G. Vitillo, F. Bonino, M. Manzoli, C.A. Grande, S. Bordiga, New insights into UTSA-16, Phys. Chem. Chem. Phys. 18 (2016) 220–227, https://doi.org/10.1039/C5CP05905D.
[32] V.I. Agueda, J.A. Delgado, M.A. Uguina, P. Brea, A.I. Spjelkavik, R. Blom, C.A. Grande, Adsorption and diffusion of H2, N2, CO, CH4 and CO2 in UTSA-16 metal-organic framework extrudates, Chem. Eng. Sci. 124 (2015) 159–169, https://doi.org/10.1016/j.ces.2014.08.039.
[33] Y. Shen, Z. Li, L. Wang, Y. Ye, Q. Liu, X. Ma, Q. Chen, Z. Zhang, S. Xiang, "Cobalt–citrate framework armored with graphene oxide exhibiting improved thermal stability and selectivity for biogas decarburization, J. Mater. Chem. A 3 (2015) 593–599, https://doi.org/10.1039/C4TA04770B.
[34] J. Binns, K.V. Kamenev, K.E.R. Marriott, G.J. McIntyre, S.A. Moggach, M. Murrie, S. Parsons, A non-topological mechanism for negative linear compressibility, Chem. Comm. 52 (2016) 7486–7489, https://doi.org/10.1039/C6CC02489K.
[35] V. Middelkoop, A. Vamvakeros, D. de Wit, S.D.M. Jacques, S. Danaci, C. Jacquot, Y. de Vos, D. Matras, S.W.T. Price, A.M. Beale, 3D printed Ni/Al2O3 based catalysts for CO2 methanation - a comparative and operando XRD-CT study, J. CO2 Util. 33 (2019) 478–487, https://doi.org/10.1016/j.jcou.2019.07.013.
[36] A. Vamvakeros, S.D.M. Jacques, M. Di Michiel, D. Matras, V. Middelkoop, I.Z. Ismagilov, E.V. Matus, V.V. Kuznetsov, J. Drnec, P. Senecal, A.M. Beale, 5D operando tomographic diffraction imaging of a catalyst bed, Nature Commun. 9 (2018) 4751, https://doi.org/10.1038/s41467-018-07046-8.
[37] V. Middelkoop, K. Coenen, J. Schalck, M. Van, Sint Annalamd, F. Gallucci, 3D printed versus spherical adsorbents for gas sweetening, Chem. Eng. J. 357 (2019) 309–319, https://doi.org/10.1016/j.cej.2018.09.130.
[38] V. Middelkoop, T. Slater, M. Florea, F. Neatu, S. Danaci, V. Onyenkeadi, K. Boonen, B. Saha, I.-A. Baragau, S. Kellici, Next frontiers in cleaner synthesis: 3D printed graphene-supported CeZrLa mixed-oxide nanocatalyst for CO2 utilisation and direct propylene carbonate production, J. Cleaner Prod. 214 (2019) 606–614, https://doi.org/10.1016/j.jclepro.2018.12.274.
[39] G. Ashiotis, A. Deschildre, Z. Nawaz, J.P. Wright, D. Karkoulis, F.E. Picca, J. Kieffer, The fast azimuthal integration Python library: pyFAI, J. Appl. Cryst. 48 (2015) 510–519, https://doi.org/10.1107/S1600576715004306.
[40] A. Vamvakeros, S.D.M. Jacques, M. Di Michiel, V. Middelkoop, C.K. Egan, R.J. Cernik, A.M. Beale, Removing multiple outliers and single-crystal artefacts from X-ray diffraction computed tomography data, J. Appl. Cryst. 48 (2015) 1943–1955, https://doi.org/10.1107/S1600576715020701.
[41] J. Kieffer, S. Petitdemange, T. Vincent, Real-time diffraction computed tomography data reduction, J. Synchrotron Radiat. 25 (2018) 612–617, https://doi.org/10.1107/s1600577518000607.
[42] A. Vamvakeros, nDTomo Software Suite, Github, 2018.
[43] M. Thommes, K. Kaneko, A.V. Neimark, J.P. Olivier, F. Rodriguez-Reinoso, J. Rouquerol, K.S.W. Sing, Physisorption of gases, with special reference to the evaluation of surface area and pore size distribution (IUPAC Technical Report), Pure App. Chem. 87 (2015) 1051–1069, https://doi.org/10.1515/pac-2014-1117.
[44] M. Kriesten, J.V. Schmitz, J. Siegel, C.E. Smith, M. Kaspereit, M. Hartmann, Shaping of flexible metal-organic frameworks: combining macroscopic stability and framework flexibility, Eur. J. Inorg. Chem. 2019 (2019) 4700–4709, https://doi.org/10.1002/ejic.201901100.
[45] D. Bazer-Bachi, L. Assié, V. Lecocq, B. Harbuzaru, V. Falk, Towards industrial use of metal-organic framework: Impact of shaping on the MOF properties, Powder Technol. 255 (2014) 52–59, https://doi.org/10.1016/j.powtec.2013.09.013.
[46] J. McEwen, J.-D. Hayman, A.O. Yazaydin, A comparative study of CO_2, CH_4 and N_2 adsorption in ZIF-8, Zeolite-13X and BPL activated carbon, Chem. Phys. 412 (2013) 72–76, https://doi.org/10.1016/j.chemphys.2012.12.012.
[47] F.A. Abdul Kareem, A.M. Shariff, S. Ullah, N. Mellon, L.K. Keong, Adsorption of pure and predicted binary (CO_2:CH_4) mixtures on 13X-zeolite: equilibirum and kinetic properties at offshore conditions, Microp. Mesop. Mater. 267 (2018) 221–234, https://doi.org/10.1016/j.micromeso.2018.04.007.
[48] N. Stiles Wilkins, J.A. Sewada, A. Rajendran, Measurement of competitive CO_2 and H_2O adsorption on zeolite 13X for post-combustion CO_2 capture, Adsorption 26 (2020) 765–779, https://doi.org/10.1007/s10450-020-00199-3.